Lawrence Berkeley National Laboratory

Title

Extracellular Proteins Limit the Dispersal of Biogenic Nanoparticles

Permalink

https://escholarship.org/uc/item/4z8085jh

Authors

Moreau, John W.
Weber, Peter K.
Martin, Michael C.
et al.

Publication Date

2007-04-27

Peer reviewed

1

Extracellular Proteins Limit the Dispersal of Biogenic Nanoparticles

3

John W. Moreau[1,*,+], Peter K. Weber[2], Michael C. Martin[3], Benjamin Gilbert[4],

Ian D. Hutcheon[2] and Jillian F. Banfield[1,5]

[1]Department of Earth and Planetary Science,

University of California Berkeley, Berkeley, CA, USA

[2]Glenn T. Seaborg Institute, Lawrence Livermore National Laboratory, Livermore, CA,

USA

[3]Advanced Light Source, Lawrence Berkeley National Laboratory, Berkeley, CA, USA

[4]Earth Science Division, Lawrence Berkeley National Laboratory, Berkeley, CA, USA

[5]Department of Environmental Science, Policy, and Management, University of

California Berkeley, Berkeley, CA, USA

* Current Address: United States Geological Survey Water Resources Division, 8505

Research Way, Middleton, WI, USA 53562

[+] Corresponding author: jwmoreau@usgs.gov

Summary: Proteins are trapped within dense aggregates of bacterially formed metal-sulfide nanoparticles, and may have played a key role in the aggregation process.

High spatial-resolution secondary ion microprobe spectrometry, synchrotron radiation Fourier-transform infrared spectroscopy and polyacrylamide gel analysis demonstrate the intimate association of proteins with spheroidal aggregates of biogenic zinc sulfide nanocrystals, an example of extracellular biomineralization. Experiments involving synthetic ZnS nanoparticles and representative amino acids indicate a driving role for cysteine in rapid nanoparticle aggregation. These findings suggest that microbially-derived extracellular proteins can limit dispersal of nanoparticulate metal-bearing phases, such as the mineral products of bioremediation, that may otherwise be transported away from their source by subsurface fluid flow.

Introduction

Sulfate-reducing bacteria can lower the concentrations of metals in anoxic waters by sequestering metals into nanoparticles (e.g., *1-3*). However, these particles are potentially highly mobile, due to their small size (*4*), and can redissolve quickly if conditions change (*5*). Sulfide nanoparticles may be less than 2 nm in diameter, comparable in size to aqueous molecular clusters (*6*); most are 2 to 6 nm (*2, 7*). Aggregation can restrict nanoparticle transport by inducing settling (*8, 9*), and drive crystal growth (leading to decreased solubility) (cf. *10, 11*). Some organics can promote aggregation. Amine-bearing molecules, for example, have been shown to organize

1   sulfide nanoparticles into semiconductor nanowires (*12*). In this study, we investigated

2   the hypothesis that natural organic matter contributes to the formation of densely

3   aggregated nanoparticulate ZnS spheroids, and is preserved in nanometer-scale pores (*7*).

4   We use microanalytical and direct isolation approaches to analyze nanoparticle

5   aggregates formed in natural sulfate-reducing bacterial biofilms (*7, 13*). We also

6   experimentally evaluate the potential for various amino acids to induce rapid aggregation

7   of metal-sulfide nanoparticles.

8   We examined sulfate-reducing bacteria-dominated biofilms collected from the

9   Piquette lead and zinc mine, a flooded system (pH ~7, T°C ~8) in southwestern

10   Wisconsin, USA (*13*). Ultramicrotomed biofilm sections that contain spheroidal

11   aggregates of biogenic ZnS nanoparticles (Figs. S1-S4) were imaged with transmission

12   electron microscopy (TEM), prior to in situ elemental microanalysis with secondary ion

13   mass spectrometry at a spatial resolution of ~50 nm (NanoSIMS) (*14*). Nitrogen in the

14   samples is detected by NanoSIMS as CN^-, NO^-, and NS^- secondary ions, and is quantified

15   by comparison to reference samples (*14, 15*).

16   Comparison of TEM images with NanoSIMS sulfur distribution maps

17   demonstrates that ZnS spheroids are the only structures within the biofilm that contain

18   significant S concentrations (Figs. 1A, C). The composite NanoSIMS data show the

19   intimate association of N with biofilm ZnS (Figs. 1A, C); N is present throughout these

20   aggregates at significantly higher levels than in abiotic ZnS reference materials (Figs. 1D,

21   E). Pores in the ZnS spheroids appear as low diffraction-contrast features in TEM

22   images, due to a lower concentration of sphalerite nanoparticles (Fig. S2). Porous

23   regions are associated with the highest N concentrations (Figs. 1B, C). Nitrogen

1   concentration measurements for individual spheroids varied by 14% (relative standard

2   deviation, n = 134), compared to an average measurement precision of 4%, for individual

3   ZnS aggregates with an average diameter of 700 nm. We estimate an average nitrogen

4   concentration for all analyzed ZnS spheroids of 1.6 wt%, with a 95% confidence interval

5   of 0.8 to 3 wt% (*14*). By comparison, the average nitrogen concentration of synthetic

6   ZnS aggregates is approximately 100 times lower.

7   The small nitrate concentration of mine water (~3 μg/g) is removed from the

8   biofilm during sample processing, and was therefore not expected to be the source of N in

9   ZnS. To test this prediction, we analyzed the spheroids for NO^- relative to CN^- (*14*). The

10   CN^-/NO^- ratio for a reference sample of KNO_3 dissolved in graphite (*14*) ranges from <1

11   to 200, with a median ratio of approximately 6. The average CN^-/NO^- ratio of bacterial

12   spores, an organic nitrogen reference, was 2950 ± 520 (s.d.). The average CN^-/NO^- ratio

13   of the biofilm ZnS was 3300 ± 870 (s.d.). Measurement precision for CN^-/NO^- in the

14   biofilm ZnS is similar to sample variability because of low NO^- secondary ion intensities.

15   Based on these analyses, we conclude that nitrogen in the biofilm ZnS is present neither

16   as nitrate nor nitrite, and is therefore organic in nature (*14*). This conclusion is further

17   supported by the presence of amide absorption features in the infrared spectra discussed

18   below. We note that from the average N content of ZnS estimated above, and taking an

19   average amino acid N concentration of approximately 11 wt%, the ZnS spheroids contain

20   approximately 14 wt% amino acids.

21   Areas with cell-like morphologies enriched in N (Fig. 1) and P (Fig. S8) are

22   interpreted as being either whole or degraded microbial cells. These features are

23   morphologically distinct compared to ZnS spheroids, arguing against spheroid formation

1   by nanoparticle encrustation and infilling of cells. We infer that the spheroids formed by

2   aggregation of biogenic ZnS nanoparticles (*13*) with extracellular polypeptides or

3   proteins. This process may have involved adsorption of amino-acids or peptides on to

4   nanoparticle surfaces (e.g., *16*), or co-aggregation of protein molecules and nanoparticles.

5   High N concentrations along the surfaces of some aggregates suggest protein-rich regions

6   (Figs. 1B, C).

7   Synchrotron-based Fourier-transform infrared spectroscopy (SR-FTIR), with

8   roughly 10 µm spatial resolution, was used to characterize organics associated with

9   biofilm ZnS aggregates (*14*). SR-FTIR analysis revealed that absorptions at

10   approximately 1580 cm^{-1} and 1640 cm^{-1} are only associated with ZnS spheroid-rich

11   regions of the biofilm (Fig. 2). These absorption features are well described for the amide

12   II and amide I vibration modes, respectively, and characteristic of polypeptide- and/or

13   protein-derived amino acids (*17*). Analyses of the spheroid-rich regions of biofilm varied

14   by a few percent in the relative magnitudes of amide I and II absorptions. The SR-FTIR

15   data confirm that the N detected by NanoSIMS analysis of spheroids is organic, and

16   support an origin in polypeptides or proteins.

17   Proteins were directly extracted from density-separated fractions dominated by

18   either organic biofilm components or ZnS spheroids (*14*; Fig. S6). Proteins from the

19   biofilm fraction produce faint bands when reacted with protein-specific stains in 4-10%

20   polyacrylamide gels at molecular weights of ~37 kDa and ~48 kDa (*14*; Fig. 3). In

21   contrast, the ZnS-enriched fraction yielded a strong band at ~37 kDa, suggesting that the

22   nitrogen detected by NanoSIMS and SR-FTIR is associated with protein(s) of this

23   molecular mass. It was not possible to characterize the protein(s) further due to their low

1 concentration and biofilm sample accessibility (*13*). However, we note that the observed

2 mass lies within the mass range of bacterial proteins known to bind certain metals (e.g.,

3 *18-20*), and genes for these proteins have been reported in some sulfate-reducing bacteria

4 (cf. *21-23*). We speculate, therefore, that the ZnS-associated protein(s) found in this

5 study may serve a metal-binding function.

6   In some aggregates, NanoSIMS data indicate overlapping N and S distributions,

7 implying the presence of fine-scale mixtures of ZnS nanoparticles and protein-rich

8 organic matter. Known bacterial metal-binding proteins bind zinc and other potentially

9 toxic metals (e.g., Cd, Cu), primarily at cysteine residues in proximity to OH^- groups

10 (*24*). Experimental evidence shows that cysteine also binds strongly to ZnS nanoparticles

11 and limits their size to < ~5 nm (*25*), and thiol groups bind strongly with sulfur-deficient

12 surface Fe(II) atoms in pyrite (FeS_2) (*16*). The conditional stability constant for mono-

13 ligand cysteine-Zn^{2+} complexation in low ionic strength solutions (= 0.1 M_c) at 20-25 °C

14 is more than 4 orders of magnitude larger than those of all the other amino acids tested

15 except for lysine, for which the constant is about 2 orders of magnitude larger (*14,* Table

16 S1). These observations suggest that cysteine or cysteine-rich polypeptides or proteins

17 could have played a role in determining the ZnS particle size and aggregation state.

18   We tested the efficacy of individual amino acids (100 µM) to promote

19 aggregation of synthetic 3 nm or smaller ZnS (10 µM) (*14*). The chosen amino acids

20 (alanine, aspartate, cysteine, lysine, phenylalanine, proline, and serine) possess

21 chemically distinct side-chain functional groups.   Aggregation was monitored

22 periodically using dynamic light scattering (DLS; *14*), and results showed that the

23 inorganic aggregation of ZnS at first occurred rapidly to form ~100 nm-diameter

1 aggregates, but then slowed greatly or ceased after one week (Figs. 4, S7). In contrast,

2 ZnS nanoparticles in the presence of cysteine exhibited more extensive and prolonged

3 aggregation, ultimately forming 1-10 μm-sized structures. Other amino acids had little

4 (e.g., serine) to no (e.g., proline) detectable effect on nanoparticle aggregation relative to

5 controls (Fig. S7). Cysteine in the absence of ZnS formed no measurable aggregates

6 (Fig. 4), and humic compounds added to ZnS nanoparticle suspensions did not accelerate

7 aggregation.

8 The DLS results correlate with prior studies of the adsorption of amino acids,

9 other organic ligands, and inorganic ions to the surfaces of metal chalcogenides (*16*, *26,*

10 *27*). For example, the sulfhydryl group present in cysteine and mercapto- compounds

11 exhibits strong specific binding to the surfaces of sulfide minerals and nanoparticles.

12 Similarly, serine with a terminal hydroxyl group causes somewhat more aggregation than

13 observed in control samples, as was expected from both the weaker chemical interaction

14 of this group with sulfide surfaces and the higher pK_a relative to cysteine (9.15 vs. 8.33).

15 Thus, we conclude that strong specific chemical binding is a necessary prelude to amino

16 acid- or protein-driven ZnS nanoparticle aggregation.

17 Mineral-protein mixtures with internal organization are typically considered

18 biominerals, and biominerals normally form within organisms. The structures reported

19 here represent an exception to this pattern. Proteins, peptides, and amino acids could be

20 released after cell death and scavenged by hydrophobic ZnS surfaces. Alternatively,

21 bacteria may export Zn-binding proteins for a physiological reason. Most known

22 bacterial metal-binding proteins are produced for intracellular binding and subsequent

23 export of toxic metals (*24*). In the case reported here, biofilm proteins may bind excess

aqueous Zn^{2+}, or interact with bound Zn(II) and other proteins subsequent to ZnS precipitation. In either scenario, the aggregation of metal-sulfide nanoparticles was promoted, preventing incidental uptake by (e.g., *28, 29*) or entombment of cells. From the dense, spheroidal morphologies, the rate of aggregation appears to be reaction-limited (*30*). Similar densely packed aggregates of biogenic metal-bearing nanoparticles have been reported from other metal-contaminated systems (e.g., *31*). Such aggregates in sediments could trap and possibly preserve organic molecules or their degradation products in sediments or rocks.

Microbial and chemical redox transformations of metals can result in the precipitation of metal-bearing nanoparticles across a range of environmental conditions (*32*). The aggregation state of these particles may have a strong impact on metal mobility and water quality (*33*). Our results suggest that aggregation induced by extracellular metal-binding polypeptides and proteins plays an important role in limiting nanoparticle dispersal in natural environments.

References

1. J.R. Lloyd, A.N. Mabbett, D.R. Williams, L.E. Macaskie, *Hydromet.* **59**, 327-337 (2001).

2. Y. Suzuki, S.D. Kelly, K.M. Kemner, J.F. Banfield, *Nature* **419**, 134 (2002).

3. S.L. Hockin, G.M. Gadd, *Appl. Environ. Microbiol.* **69**, 7063-7072 (2003).

4. B.D. Honeyman, *Nature* **397**, 23-24 (1999).

5. J.G. Hering, W. Stumm, In M.F. Hochella, Jr., A.F. White (Eds.), *Rev. Min. Geochem.* **23**, 427-465 (1990).

6. G.W. Luther, S.M. Theberge, D.T. Rickard, *Geochim. Cosmochim. Acta* **63**, 3159-3169 (1999).

1
2   7. J.W. Moreau, R.I. Webb, J.F. Banfield, *Amer. Min.* **89**, 950-960 (2004).
3
4   8. C. Allain, M. Cloitre, F. Parisse, *J. Colloid Interf. Sci.* **178**, 411-416 (1996).
5
6   9. S.A. Bradford, S.R. Yates, M. Bettehar, J. Simunek, *Wat. Res. Res.* **38**, 1327, doi:
7   10.1029/2002WR001340 (1996).
8
9   10. J.W. Zhang, G.H. Nancollas, In M.F. Hochella, Jr., A.F. White (Eds.), *Rev. Min.*
10   *Geochem.* **23**, 365-393 (1990).
11
12   11. W. Stumm, J.J. Morgan, Aquatic chemistry: chemical equilibria and rates in natural
13   waters (Wiley and Sons, New York, 1996), pp. 400-414.
14
15   12. Q. Lu, F. Gao, D. Zhao, *Nanotech.* 13, 741-745 (2002).
16
17   13. M. Labrenz *et al.*, *Science* 290, 1744-1747 (2000).
18
19   14. Materials and methods are available as supporting material on *Science* Online.
20
21   15. E.H. Hauri, J. Wang, D.G. Pearson, G.P. Bulanova *Chem. Geol.* **185,** 149-163 (2002).
22
23   16. J. Bebie, M.A.A. Schoonen, *Geochem. Trans* 8 (2000).
24
25   17. H.H. Mantsch, D. Chapman, *Infrared spectrosc. biomol.*, (Wiley-Liss, New York,
26   1996).
27
28   18. M.B. Khazaeli, R.S. Mitra, *Appl. Environ. Microbiol.* 41, 46-50 (1981).
29
30   19. E. Kurek, A.J. Francis, J.M. Bollag, *Arch. Environ. Contam. Toxicol.* 20, 106-111
31   (1991).
32
33   20. D.H. Nies, *J. Bact.* 174, 8102-8110 (1992).
34
35   21. N. Naz, H.K. Young, N. Ahmed, G.M. Gadd, *Appl. Environ. Microbiol.* 71, 4610-
36   4618 (2005).
37
38   22. T.A.M. Bridge, C. White, G.M. Gadd, *Microbiol.* 145, 2987-2995 (1999).
39
40   23. C.A. Blindauer *et al.*, *PNAS* 98, 9593-9598 (2001).
41
42   24. B.P. Rosen, *J. Biol. Inorg. Chem.* 1, 273-277 (1996).
43
44   25. C.L. Torres-Martinez *et al.*, *Nanotech.* 10, 340-354 (1999).
45

26. L. Ronngren, S. Sjoberg, Z. Sun, W. Forsling, P.W. Schindler, *J. Colloid Interf. Sci.* 145, 396-404 (1991).

27. W. Vogel, *Langmuir* 16, 2032-2037 (2000).

28. T. Barkay, J. Schaefer, *Curr. Opin. Microbiol.* 4, 318-323 (2001).

29. J.A. Kloepfer, R.E. Mielke, J.L. Nadeau, *Appl. Environ. Microbiol.* 71, 2548-2557 (2005).

30. G.A. Waychunas, In J.F. Banfield, A. Navrotsky (Eds.) *Rev. Min. Geochem*. 44, 105-166 (2001).

31. J.S. Ahn, Y.S. Park, J.Y. Kim, K.W. Kim, *Environ. Geochem. Health* 27, 147-157 (2005).

32. M.F. Hochella, Jr., *Geochim. Cosmochim. Acta* 66, 735-743 (2002)

33. M.S. Diallo, N. Savage, *J. Nanopart. Res.* 7, 325-330 (2005).

1 **Figure Captions:**
2
3 **Figure 1: NanoSIMS secondary ion images showing C, N and S distributions in an**
4 **ultramicrotomed TEM section of biofilm.** (**A**) Composite element distribution map
5 (~10 µm x 10 µm) of ^{12}C (blue), ^{12}C^{14}N *for N* (green), and ^{32}S (red). Colors reflect the
6 proportion each species. For example, uniformly red regions represent relatively pure ^{32}S
7 (as ZnS), while orange or yellow regions indicate the presence of increased levels of
8 nitrogen. Cyan regions indicate the presence of both carbon and nitrogen, with little to
9 no sulfur (no ZnS). (**B**) TEM image of several conjoined ZnS spheroidal aggregates. (**C**)
10 NanoSIMS composite element distribution map of (B).   (D) NanoSIMS composite
11 element distribution map of ultramicrotomed Balmat ZnS. (E) NanoSIMS composite
12 element distribution map of synthetic nanoparticulate ZnS. (F) Color box plots of the
13 relative ion abundances displayed in (A, C, D and E). Primary colors and maximum ion
14 counts are noted for each species along each axis; all axes are linear with respect to ion
15 counts. In the left box ("binary"), only binary ion compositions (one or two species) are
16 shown; in the right box ("ternary"), only primary (the species corresponding to each axis)
17 and ternary ion compositions (three species) are shown. Black and white "corners"
18 correspond to points of minimum and maximum ion counts, respectively, for all three
19 species. All scale bars are 1 µm. Figs. S8-S10 (*14*) present grayscale versions of Figs.
20 1A, C, and D, respectively.
21
22 **Figure 2. SR-FTIR transmission spectra of biogenic ZnS aggregates (black) and**
23 **background biofilm (gray).** Amide I (~1640 cm^{-1}) and II (~1580 cm^{-1}) absorption
24 features are diagnostic of amino-acid associated bond vibrations in polypeptides and/or
25 proteins.
26
27 **Figure 3:   Composite SDS-PAGE gel electrophoresis image of biofilm and ZnS**
28 **protein extractions.** SyproOrange and colloidal silver molecular weight standards (far
29 left and right lanes, respectively). (**A**) Extraction from the biofilm organic fraction
30 stained with SyproOrange. (**B**) Extraction of the ZnS spheroid fraction stained with
31 SyproOrange. (**C and D**) Replicate extractions of biofilm organic fraction stained with
32 silver. (**E and F**) Replicate extractions of ZnS spheroids fraction stained with silver.
33 Numbers are molecular masses in kilodaltons (kDa).
34
35 **Figure 4:   Size distribution curves from dynamic light scattering (DLS) data**
36 **acquired in ZnS nanoparticles aggregation experiments.** (**A**) Control experiments. 10
37 uM ZnS nanoparticles alone (solid lines) aggregate within 1 day to form ~100 nm radius
38 clusters that exhibit little further growth over the 5 day period. 100 µM cysteine alone
39 (dashed lines) gives a very weak DLS signal with is no consistent trend in size
40 distribution. (**B**) In the presence of both 10 µM ZnS and 100 µM cysteine, sustained
41 aggregation occurs over the 7 day period, resulting in aggregates that are more than 1
42 order of magnitude larger than the initial clusters. DLS correlation functions from which
43 size distributions were derived are shown in Fig. S7.
44
45

1　**Supplementary Materials and Methods:**

2

3　*Transmission electron microscopy (TEM)/Secondary ion mass spectrometry (SIMS)*

4　*biofilm sample preparation:*

5

6　Samples of biofilm were fixed with 4% glutaraldehyde, as described previously (*S1*).

7　TEM images (Fig. S4) confirm that, because the sectioning resin neither displaces nor

8　damages fine-scale biofilm features, ultramicrotomed samples of biofilm used for TEM

9　imaging were also suitable for SIMS analyses.

10

11　*Secondary Ion Mass Spectrometry (SIMS):*

12

13　SIMS was performed using the Lawrence Livermore National Laboratory NanoSIMS 50

14　(Cameca, Gennevilliers Cedex, France). The measurements were made with a 0.2 to 0.7

15　pA, 16 keV $^{133}Cs^+$ primary ion beam focused into a 50 to 100 nm diameter spot, rastered

16　over sample areas of ~10 x 10 μm^2. The isotope imaging measurements consist of 15 to

17　100 replicate scans of 256 x 256 or 512 x 512 pixels with dwell times of 1-2 ms/pixel.

18　Secondary ion intensities were collected simultaneously in multi-collection mode using

19　three different collector configurations, $[^{12}C^-, \ ^{12}C^{14}N^-, \ ^{31}P^-, \ ^{32}S^-]$, $[^{12}C^-, \ ^{12}C^{14}N^-, \ ^{14}N^{16}O^-,$

20　$^{32}S^-, \ ^{14}N^{32}S^-]$ and $[^{12}C^-, \ ^{12}C^{14}N^-, \ ^{32}S^-, \ ^{14}N^{32}S^-]$. A mass resolving power of ~4000 was

21　used. Samples were also simultaneously imaged using secondary electrons. The $^{12}C^{14}N^-$

22　$/^{14}N^{16}O^-$ ratio in the biofilm and ZnS spheroids was compared to this ratio in a sample of

23　KNO_3 dissolved in graphite as a nitrate reference (~0.3 wt% KNO_3), and bacterial spores

24　as an organic nitrogen reference, to test for significant levels of nitrate in the ZnS

25　spheroids. Nitrogen concentration in the ZnS aggregates was estimated based on a

26　relative sensitivity factor for NS^- (RSF_{NS}) of 4.2 x 10^{24} cm^{-3} for NS^- relative to S^- in ZnS

27　(*S2*). The ZnS standard was produced by implanting N into a ZnS crystal with 150-keV

28　at a fluence of 1 x 10^{14} atoms/cm^2. The abundance of N (atoms per cm^3) in ZnS (C_N) is

29　estimated from:

30　$$C_N = RSF_{NS} * I_{NS}/I_S,$$

31

32　where I_{NS} and I_S are ion count rates for NS^- and S^- corrected for the abundances of ^{14}N

33　and ^{32}S relative to total N and S (*S3*). The abundance of N in ZnS (wt%) is calculated

34　from C_N, Avogadro's number, the atomic mass of N, and the density of ZnS. The

35　estimate of absolute abundance of N in the ZnS aggregates is given a factor of two

36　uncertainty to allow for the RSF_{NS} being generated on a different SIMS instrument;

37　actual accuracy is likely higher. Data for CN^- are used in the figures because CN^- has

38　approximately 100 times higher intensity than NS^- (Fig. S11) and therefore provides

39　higher clarity images.

40

41　Composite multi-element images were constructed using Photoshop (Adobe) and the

42　NanoSIMS data analysis software, *L'image* (developed by L. Nittler, Carnegie Institution

43　of Washington, Washington, D.C., USA). Grey-scale $^{12}C^-$, $^{12}C^{14}N^-$ and $^{32}S^-$ intensity

44　images generated by *L'image* (e.g. Figs. S8-S10) were assigned to blue, green and red

45　channels, respectively, in Photoshop RGB (red/green/blue) image files.   Therefore,

primary colors in the images represent the presence of only one of the elements, whereas "binary" or "ternary" colors represent mixtures of two or three elemental components, respectively. Black indicates areas of no data (i.e. holes in the TEM section). The color box plot "key" to Fig. 1 (F) represents in three-dimensional space the surfaces of possible binary and ternary mixtures of the three colors (i.e. elements). The significance of measurements obtained via NanoSIMS analyses of biofilm ZnS, for >1,000 regions-of-interest (ROIs) of approximately 180 nm^2 each, was determined by comparison to NanoSIMS analyses of natural and synthetic ZnS reference materials (Figs. 1D, E). In addition to a natural single-crystal ZnS standard (Balmat sphalerite, NBS123) (Fig. 1D), nanoparticulate ZnS synthesized (*S4*) by H. Zhang (UC Berkeley) (Fig. 1E) was used to represent a similarly structured (i.e., nanocrystalline) pure ZnS reference material for comparison.

In the course of analysis by dynamic SIMS methods such as NanoSIMS, the high energy primary ion beam breaks chemical bonds in the sample. Dimers produced in the course of primary beam sputtering originate from atoms in the sample, and therefore, at a minimum, it is possible to determine if elements are associated with each other at the scale of the primary beam. To some extent, dimers will come from bonded atoms or be affected by chemical bonding in the sample (*S5*). Therefore, we analyze organic and nitrate reference materials for CN^- and NO^- to determine empirically if the relative yield of these two dimers can be used to constrain the nature of N in the ZnS aggregates. The $^{12}C^{14}N^-/^{14}N^{16}O^-$ data for the organic standard and the biofilm ZnS are well constrained around 3000, within the range of counting statistics. The $^{12}C^{14}N^-/^{14}N^{16}O^-$ data for the inorganic reference material, KNO_3 dissolved in graphite, is more scattered and highly skewed (skewness = 3.2), with over 75% of the data below a ratio of 20 and less than 10% over 50 (Fig. S5A). These data are from two 10 x 10 μm^2 fields, subdivided into 169 ROIs each, and provide a reference for NO_3^- associated with carbon. The NO_3^- abundance in the graphite is heterogeneous (mean of ~0.3 wt.%), providing a range of concentrations for comparison to other samples. The experiment shows that even in the case of intimate association of NO_3^- with carbon at low concentrations at sputtering equilibrium, the relative yield of CN^- to NO^- is at least a factor of 10 lower than observed in the organic sample and the biofilm ZnS aggregates (Fig. S5B). At higher concentrations relative to C, the CN/NO ratio is below 1. We take this experiment as evidence that the N in the ZnS aggregates is not present as nitrate or nitrite, and therefore is organic in nature.

Synchrotron-radiation Fourier transform infra-red spectroscopy (SR-FTIR):

SR-FTIR is capable of detecting and differentiating amongst nucleic acids, lipids, amino acids, and polysaccharides (*S6*). The spatial resolution of SR-FTIR, coupled with optical microscopy, is diffraction limited, or between 2 and 10 μm in the mid-infrared (*S7*). SR-FTIR analyses were conducted on uncoated ultramicrotomed sections of the same biofilm samples used for NanoSIMS analyses. The location of the synchrotron probe relative to targets selected with optical microscopy was calibrated using IR-sensitive targets on

1 standards. Background spectra were obtained and used as reference spectra for both
2 samples and standards to remove atmospheric H_2O and CO_2 absorptions.
3
4 *Biofilm/ZnS separation and total protein extraction:*
5
6 Biofilm samples were homogenized by repeated pipetting action through a series of
7 sterile syringe needles of increasingly smaller inner-bore diameter (18-, 21- and 22-
8 gauge, respectively, for approximately 20 minutes each). Homogenized biofilm slurries
9 were then pelleted by centrifugation, re-suspended in lithium polytungstate solution
10 (LST) of density ~2.8 g cm^{-3} (Geoliquids, Prospect Heights, IL, USA), and then subjected
11 to further low-speed centrifugation (~5 mins at 1000 rpm) in autoclaved microcentrifuge
12 tubes (Eppendorf, Hamburg, Germany). ZnS-rich biofilm fragments (r ~4.1 g cm^{-3}) were
13 easily pelleted at the bottom of LST-filled tubes during centrifugation, while ZnS-poor
14 biofilm fragments rose to the top of the LST solution to be re-pipetted into new tubes.
15 This process of low-speed centrifugation, density-based fractionation, collection and re-
16 suspension was repeated several times, until no further separation of ZnS-rich and ZnS-
17 poor biofilm fractions was observed. Both fractions were transferred a final time by
18 pipette to clean tubes of nuclease-free water, and then pelleted, washed and re-suspended
19 6-8 times, to remove all traces of LST. Each resulting fraction represents a subsample of
20 biofilm or ZnS spheroids with greatly increased relative concentrations of organic matter
21 or ZnS, respectively. This method avoids the use of surfactants or solvents that might
22 solubilize and destroy organic biomolecules, including nucleic acids and proteins. Each
23 "density fraction" from the separation process was pelleted and re-suspended a final time
24 in 2% sodium dodecyl sulfate (SDS) solution for one hour at room temperature with
25 gentle mixing to denature any proteins (*S8*).
26
27 *Protein gel electrophoresis:*
28
29 Molecular weight standard "ladders" were run on both sides of all sample gel lanes to
30 correct for horizontal distortions commonly produced during gel electrophoresis. Protein
31 extractions were analyzed using two different molecular weight ladders and two different
32 staining methods, for comparison of sample protein size/weights and staining
33 efficiencies. One set of gels was reacted with a silver-based stain (BioRad, Hercules,
34 CA, USA) (*S9*), and Kaleidoscope (BioRad) pre-stained molecular weight ladders were
35 used to calibrate the weight/size of protein bands. These gels were imaged using a
36 standard Epson scanner. The second set of gels was stained with SyproOrange (BioRad),
37 a UV-fluorescent dye that specifically binds to proteins (*S10*), and protein bands were
38 calibrated to broad-range SyproOrange molecular weight ladders. These gels were
39 imaged using a UV-VIS light gel documentation system (BioRad). Both SyproOrange
40 and silver staining can be used to detect =10 ng of protein.
41
42 *ZnS nanoparticle synthesis:*
43
44 Nano-ZnS was synthesized by the reaction of 150 mM ZnCl$_2$ and aqueous sulfide, which
45 were dissolved separately into 200 ml of ultra-pure (0.1 μm pore-size double-filtered

MilliQ; Millipore, Billerica, MA, USA) DI water and reacted drop wise under constant stirring for 1.5 hr (*S5*).

ZnS nanoparticle/amino acid aggregation experiments:

The initial size of ZnS precipitates was determined to be = 3 nm diameter using a UV-vis spectrometer (Ocean Optics, Dunedin, FL, USA) calibrated for ZnS particle size using published TEM observations (*S11*). The following experimental conditions were established in separate glass flasks: (a) "blanks" (ultrapure water only), (b) ZnS nanoparticles only, (c) a single amino acid only and (d) ZnS nanoparticles plus a single amino acid. All incubation flasks were (in the following order) detergent-washed, rinsed with MilliQ water three times, acid-washed in 0.1N HCl overnight, rinsed five times with MilliQ water, and sealed with parafilm, prior to the experiment. After the addition of any reagents, flasks were resealed with parafilm and kept sealed during the experiment between sampling times. All flasks were gently stirred throughout the experiment by acid-washed Teflon-coated magnetic stirrer bars. 1 ml aliquots from each experimental condition were taken at 0, 0.5, 1, 3, 5, and 7 days of reaction progress. Between sample measurements, 0.5 ml of 0.1 N HCl was flushed through the sample line and chamber, followed by 3 ml of ultrapure water, to avoid cross-contamination of samples. Three measurements of 40 – 60 accumulations each were obtained per analysis at each sampling time point.

The amino acids chosen for these aggregation experiments represent the following classes of structures and functional groups: alanine (nonpolar, aliphatic), aspartate (acidic, negatively charged), cysteine (polar, uncharged, thiol-bearing), lysine (basic, positively charged), phenylalanine (aromatic), proline (polar, uncharged, imine-bearing), and serine (polar, uncharged, hydroxyl-bearing). Their conditional stability constants for mono-ligand complexation of aqueous Zn^{2+} are given in Table S1, from data collected by Martell and Smith (*S12*).

Dynamic light scattering (DLS) analysis:

DLS analysis was performed with a PD-Expert Workstation (Precision Detectors, Bellingham, MA, USA) fitted with a quartz flow-through cell maintained at 25 °C. Laser light (685 nm wavelength) scattered through 135° was sent via glass fiber to an optical correlator. The DLS correlation function is a direct measurement of the diffusion coefficient(s) of objects suspended in a solvent. For specific values of solvent viscosity and refractive index, an effective hydrodynamic radius, R_H, of the object(s) can be calculated (*S13*). In the present case, we observed light scattering from aggregates of ZnS nanoparticles. Because the exact shape and hydrodynamic properties of nanoparticulate aggregates are not well known, there may be systematic differences between the calculated R_H and spatial dimensions observed by alternative techniques (such as electron microscopy). Determination of the distribution of ZnS aggregate sizes was performed using proprietary Precision Detectors software (PrecisionDeconvolve) that employs a regularization algorithm (*S14*) to seek a smooth, non-negative size distribution function that provides the best fit to the data. Low noise DLS data analyzed

1 with this method can resolve multimodal distributions, provided the diffusion coefficients
2 differ by greater than a factor of ~ 2.5.
3 **Supplementary Figure Captions:**
4
5 **Figure S1: Field-emission scanning electron microscopy (FESEM) secondary**
6 **electron image of micron-scale spheroidal aggregates of nanocrystalline biogenic**
7 **ZnS formed in the biofilm.**
8
9 **Figure S2: HRTEM image of cross-section through spheroidal biogenic ZnS**
10 **aggregate in the biofilm.** Multiple concentric rings (3-5 nm wide, shown by white
11 arrows) of low electron density attributed to porous regions separate bands of densely
12 aggregated nanoparticulate ZnS.
13
14 **Figure S3: HRTEM images of biogenic ZnS nanoparticles formed in a biofilm of**
15 **sulfate-reducing bacteria.** (**A**) The smallest ZnS nanoparticles are crystalline, as shown
16 by {111} lattice fringes in [02-2] projection, and <2 nm-diameter. (**B**) Several
17 aggregated nanoparticles with boundaries indicated by dashed lines. (**C**) Disordered ZnS
18 aggregates contain multiple stacking faults (interpolated along pairs of white lines) that
19 give rise to wurtzite subdomains (across white line pairs) in sphalerite. (**D**) Example of
20 aggregation producing faceted surfaces and negative crystals (dashed white triangle). All
21 scale bars are 2 nm.
22
23 **Figure S4**: **TEM image of biofilm organic matter, cells and ZnS aggregates.** Stained
24 ultramicrotomed sections of biofilm show abundant ZnS spheroidal aggregates (black
25 spheroidal features with strong diffraction contrast) surrounded by biofilm organic matter
26 (white arrows), and in close proximity to cells (black arrows). Dark grey spheroidal
27 features with lighter grey cores (grey arrows) are cells surrounded by capsular organic
28 matter that has been stained with uranyl acetate and lead citrate. Scale bars are 1 μm.
29
30 **Figure S5**: $^{12}C^{14}N^-/^{14}N^{16}O^-$ **ratios of KNO$_3$ dissolved in graphite.**   (**A**) Histogram of
31 the number versus $^{12}C^{14}N^-/^{14}N^{16}O^-$ ratio for each of 338 10 x 10 μm^2 regions analyzed.
32 The distribution is highly skewed (skewness = 3.2), with over 75% below a ratio of 20
33 and less than 10% over 50. (**B**) Plot of $^{12}C^{14}N^-/^{14}N^{16}O^-$ versus $^{12}C^{14}N^-/^{12}C$ ratios for the
34 same regions in (A). $^{12}C^{14}N^-/^{14}N^{16}O^-$ ratios are, for all analyses, at least one order of
35 magnitude less than those observed in biofilm ZnS spheroids.
36
37 **Figure S6: Microcentrifuge tubes of lithium-polytungstate solution (LST), biofilm**
38 **and ZnS.** The left-hand tube shows the color of pure LST. Homogenized biofilm is
39 introduced and subjected to low speed centrifugation to separate lower and higher density
40 fractions (middle tube). Density-driven separation is iteratively repeated until no further
41 separation is achieved (right-hand tube). Material at the top of the LST solution consists
42 predominantly of biofilm organic matter, while the pellet at the bottom is concentrated in
43 ZnS spheroids.
44

Figure S7: Dynamic light scattering (DLS) data acquired during ZnS nanoparticle aggregation experiments. *Top row*: size distribution histograms. *Bottom row*: DLS correlation functions. The first column shows the data for the control experiment in which ZnS nanoparticle aggregation was observed without any amino acid added. Subsequent columns are labeled with the name of the added amino acid. We investigated the ability of the amino acids to drive nanoparticle aggregation by comparing the time-dependent cluster size with the no-amino acid control. The aggregation behavior in the presence of proline was indistinguishable from the control, and similar results were obtained for alanine and phenylalanine. Serine appeared to drive some additional aggregation relative to the control, and similar results were obtained for aspartate and lysine. Only experiments in the presence of cysteine showed extensive and prolonged aggregate formation.

Figure S8: NanoSIMS secondary ion images of biofilm with ZnS aggregates. Grayscale version of Fig. 1A in which each component element (i.e. color) is here shown separately as total counts. One additional frame has been added (*lower right*) to demonstrate the strong degree of phosphorus co-localization with only features exhibiting both increased carbon and nitrogen counts (*upper row*). Scale bars are 500 nm.

Figure S9: NanoSIMS secondary ion images of biofilm with ZnS aggregates. Grayscale version of Fig. 1C in which each component element (i.e. color) is here shown separately as total counts. One additional frame has been added (*lower right*) to again demonstrate the absence of phosphorus in ZnS spheroids. Scale bars are 500 nm.

Figure S10: NanoSIMS secondary ion images of ultramicrotomed Balmat ZnS reference standard. Grayscale version of Fig. 1D in which each component element (i.e. color) is here shown separately as total counts. Scale bars are 500 nm.

Figure S11: NanoSIMS secondary ion images of biofilm with ZnS aggregates. Grayscale version of a different region of biofilm from the same sample shown in Fig. 1A. In addition to the same component elements shown in Fig. 1, the species $^{32}S^{14}N$ is shown. Based on the significantly higher counts for $^{12}C^{14}N$ than for $^{32}S^{14}N$, the former species was used to measure the nitrogen content of ZnS spheroids and other biofilm components.

Table S1: Stability constants for various amino acids. Data are taken from (*12*), for the reaction $M + L \rightarrow ML$, where $M = Zn^{2+}$ and L = amino acid. I = ionic strength.

Supplementary References:

1. J.W. Moreau, R.I. Webb, J.F. Banfield *Amer. Min.* 89, 950-960 (2004).

2. Written communication, Robert G. Wilson, December 30, 2006.

3. R.G. Wilson, F.A. Stevie, C.W. Magee, *Secondary Ion Mass Spectrometry: A Practical Handbook for Depth Profiling and Bulk Impurity Analysis* (Wiley, New York, 1989).

4. After the method of B.R. Müller, S. Majoni, R. Memming, D. Meissner, *J. Phys. Chem. B 101*, 2501-2507 (1997).

5. G. McMahon, H. Francois Saint-Cyr, C.J. Unkefer, C. Lechene, *J. Am. Soc. Mass. Spectrom*. **17**, 1181-1187 (2006).

6. H.H. Mantsch, D. Chapman, *Infrared spectrosc. biomol.*, (Wiley-Liss, New York, 1996).

7. E. Levenson, P. Lerch, M.C. Martin, *Infrared Phys. Tech*. 49, 45-52 (2006).

8. Following the method of J. Sambrook, E.F. Fritsch, T. Maniatis, *Molecular cloning: a laboratory manual* (Cold Spring Harbor Laboratory Press, Cold Spring Harbor, 1989).

9. M. Gottlieb, M. Chavko, *Anal. Biochem.* 165, 33-37 (1987).

10. J.R. Lawrence *et al.*, *Appl. Environ. Microbiol.* 69, 5543-5554 (2003).

11. H. Zhang, B. Gilbert, F. Huang, J.F. Banfield, *Nature* 424, 1025-1029 (2003).

12. A.E. Martell, R.M. Smith, *Crit. stability constants, vol. 1: amino acids* (Plenum Press, New York, 1974).

13. S. Romer *et al., J. Appl. Crystallog.* 36, 1-6 (2003).

14. S.W. Provencher, *Comput. Phys. Comm.* 27, 229-242 (1982).
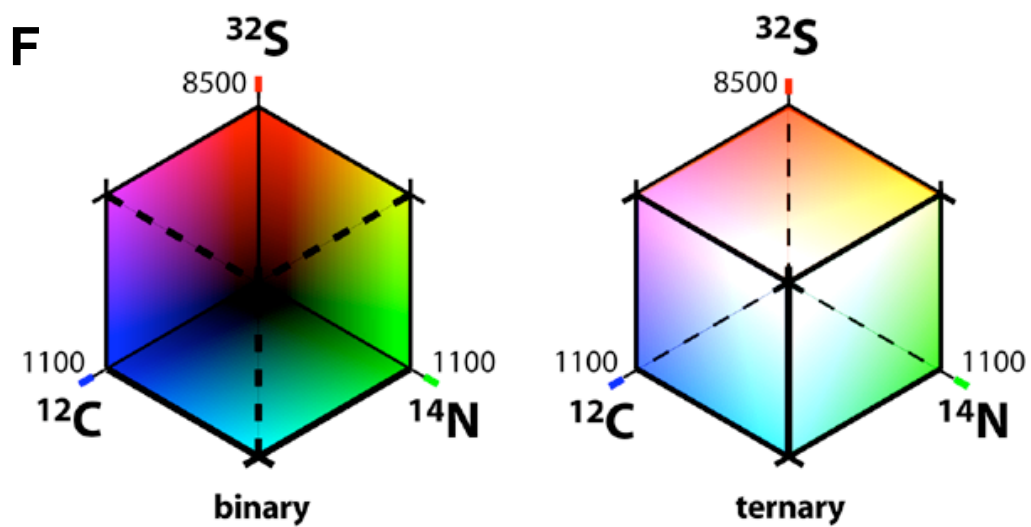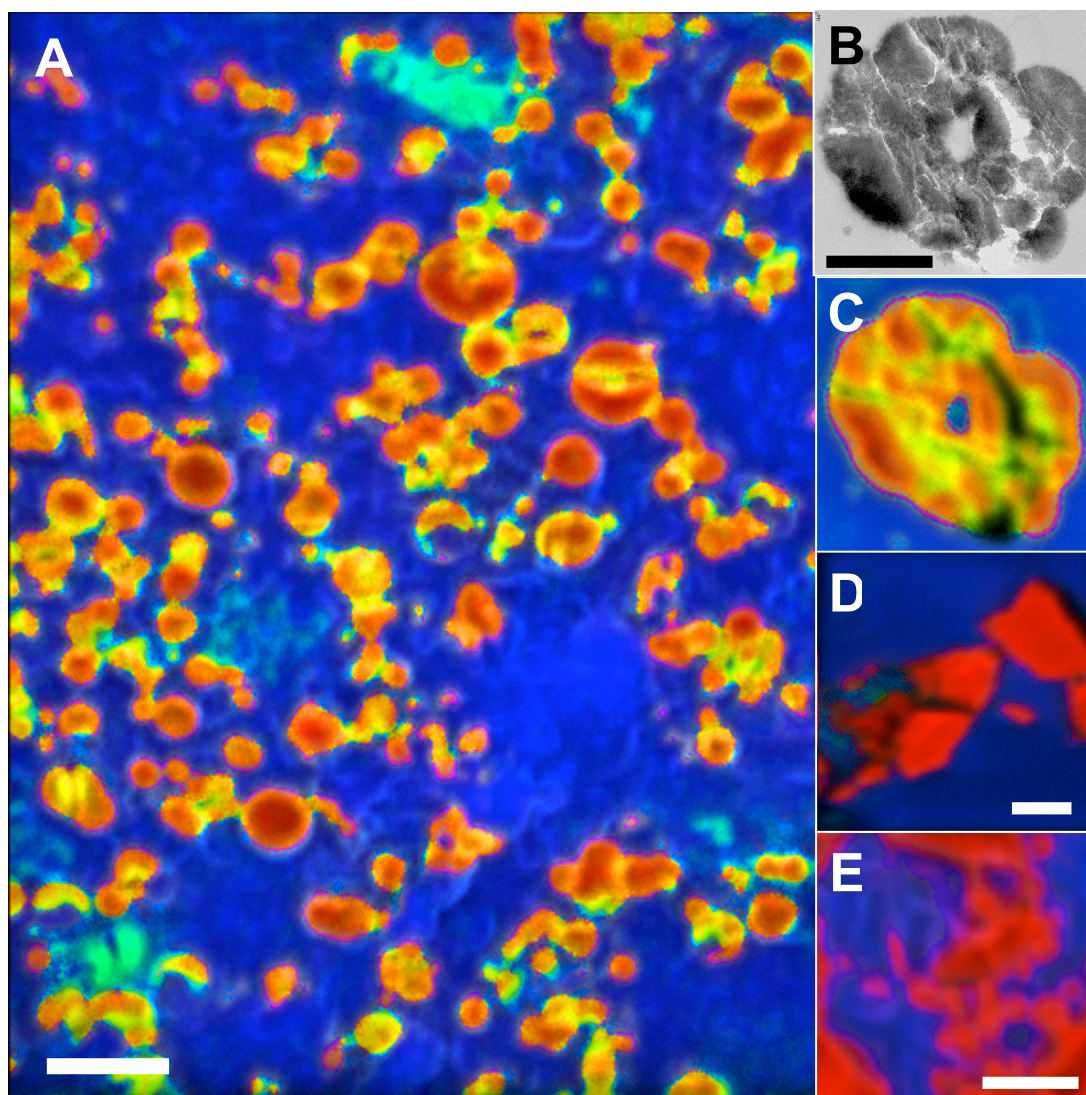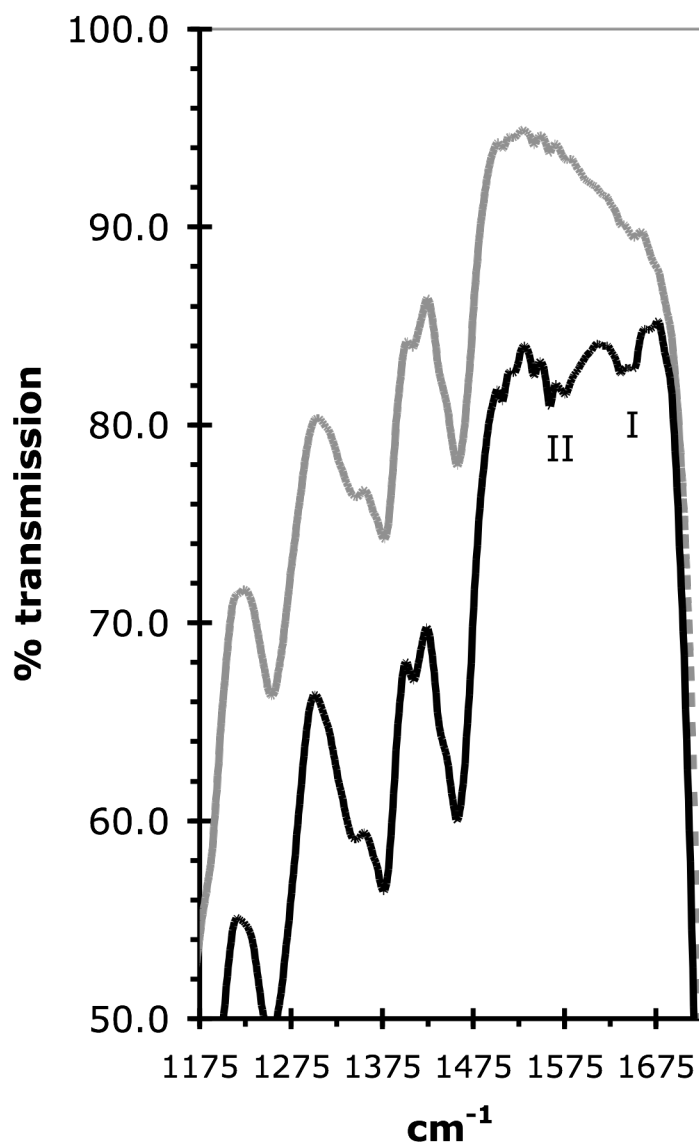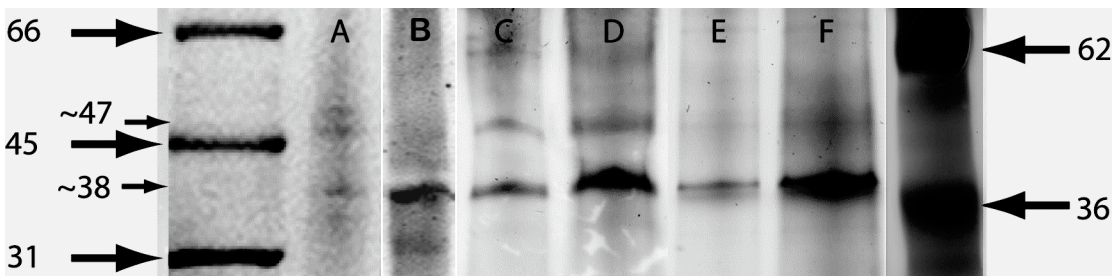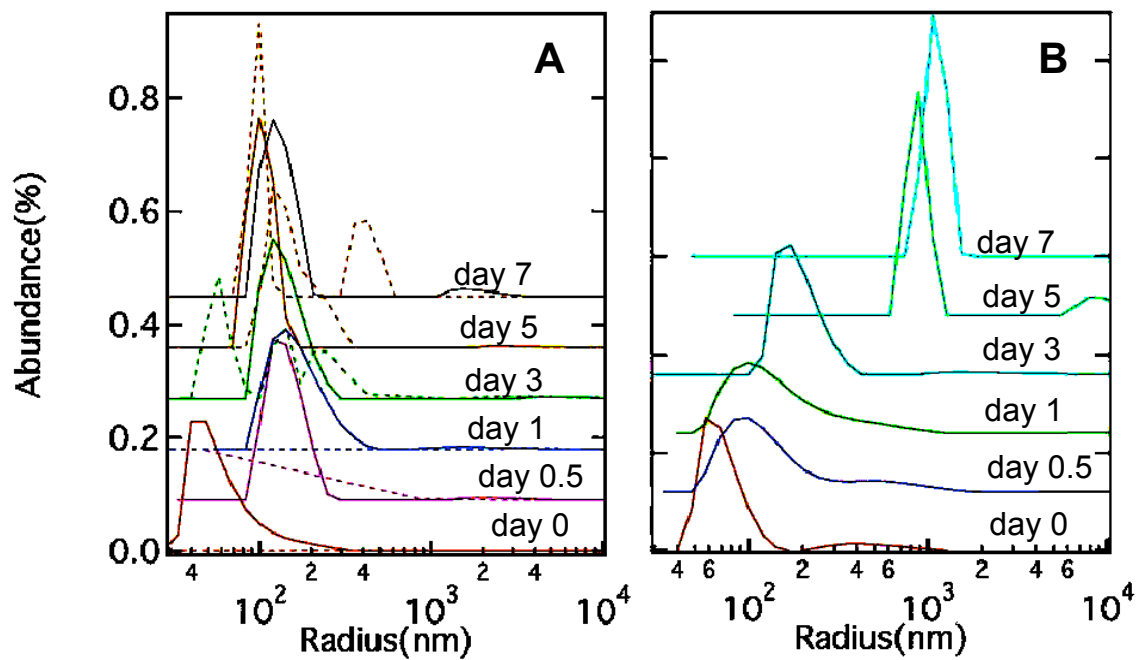
1
2
3

Figure 1

1 **Figure 2**
2
3
4
5
6
7
8
9
10
11
12
13
14
15
16
17
18
19
20
21
22
23
24
25
26
27
28
29
30
31
32
33
34
35
36
37
38
39
40
41
42
43
44
45

Figure 3

Figure 4